AIAA SciTech Forum
6-10 January 2025, Orlando, FL
AIAA SCITECH 2025 Forum

10.2514/6.2025-0810

Effect of Cross Section Scaling on the Performance of a Trussed Collapsible Tubular Mast

Jacob Tersigni* and Francisco López Jiménez†
University of Colorado, Boulder, CO, USA

Michael Folkers‡, Drayton Browning§, and Thomas Murphey¶
Opterus Research and Development, Loveland, CO, USA

We present an analysis of the Solar Sail Tubular Mast (SSTM), an ultra-lightweight deployable boom architecture. The mast consists of High Strain Composite tape springs configured in a truss structure such that it is flattenable and rollable. We performed finite element simulations to rationalize the effect of different geometry parameters on the boom's stiffness and buckling behavior under axial, bending, and torsion loading conditions. Closed form approximations for bending stiffness and buckling moment in bending in terms of key design variables were developed. These analytical models were also used to constrain the design space by evaluating a large number of boom designs against design requirements, allowing designers to optimize mass efficiency and performance. The effect of uniformly scaling the boom cross-section diameter and other design variables is also explored.

I. Nomenclature

W_l	=	longeron width, m
W_b	=	batten width, m
Sc	=	cross-section scaling factor
Nb	=	number of battens
L	=	boom length, m
C	=	characteristic length for axial buckling with a force through a fixed point, m
EI	=	bending stiffness, Nm^2
P	=	point load, N
M	=	applied moment, Nm
P_{cr}	=	axial critical buckling load, N
M_{cr}	=	critical buckling moment, Nm
β	=	angle between the solar sail tension vector and the mast, radians
k	=	dimensionless buckling parameter
λL	=	effective length for buckling
ϕ	=	dimensionless shear compliance parameter
κ_s	=	shear correction coefficient
GA	=	shear rigidity, N
θ	=	beam deflection angle, radians
ϵ	=	strain, m/m
y	=	distance from the bending axis, m
l	=	bay length, m
t	=	longeron thickness, m

*Graduate Student, Ann and H.J. Smead Department of Aerospace Engineering Sciences, University of Colorado Boulder, AIAA Student Member.
†Assistant Professor, Ann and H.J. Smead Department of Aerospace Engineering Sciences, University of Colorado Boulder, AIAA Senior Member.
‡Mechanical Engineer, Opterus Research and Development.
§§Mechanical Engineer and Project Manager, Opterus Research and Development.
¶Founder CEO, Opterus Research and Development, AIAA Associate Fellow.

r = longeron radius of curvature, m
α = longeron half subtended angle, radians
EA = axial stiffness, N
δ = displacement, m
GJ = torsional stiffness, $\mathrm{Nm}^2/\mathrm{rad}$
A = cross-section area, m
μ_B = bending performance metric, $\mathrm{N}^{3/5}\mathrm{m}^{4/5}\mathrm{kg}^{-1}$

II. Introduction

Space structures often rely on deployable booms to support and deploy large structural elements in space, including solar arrays, antennas, and sails [1, 2]. Several designs leverage slender curved shells such as tape springs that can be folded elastically for stowage and that deploy by releasing the stored strain energy, without the need for external actuation. Examples include the Storable Tubular Extendible Member (STEM) boom [3], the Triangular Retractable and Collapsible (TRAC) [4], and the double-omega boom [1]. The different cross-sections of all these designs determine the allowable curvature and therefore their stowed volume, as well as their mechanical performance. For example, open cross-sections tend to have higher bending stiffness for the same weight per unit length, while closed cross-sections exhibit larger torsional stiffness and strength. As such, different applications favor different designs, based on the expected loading conditions.

Solar sails, including the Advanced Composite Solar Sail System (ACS3) launched in early 2024, use deployable booms to deploy and tension the sail. Solar sails able to provide sufficient thrust for space exploration missions require very large deployed surfaces, extremely low mass, and small stowage volume. At the same time, the booms need to provide sufficient axial, torsional, and bending stiffness and strength, which is difficult for large systems. Successful solar sail demonstrations have thus far been limited to a maximum surface area of 200 m^2 for IKAROS [5], with an area of 80 m^2 for the ACS3. However, future mission concepts, including the Solar Polar Orbiter [6], the High Inclination Solar Mission [7], and the Solar Polar Imager [8], require solar sail areas up to 10,000 m^2. These mission concepts raise the need for new, significantly longer, boom designs which maintain low mass and packaging volume.

The Solar Sail Tubular Mast (SSTM) [9] design is proposed for boom lengths on the order of tens of meters. The SSTM uses a similar cross-section shape and design principals to the Trussed Collapsible Tubular Mast (TCTM) previously designed by Opterus [10], while reducing weight by using a trussed rather than a solid cross-section. This work is a continuation on previous work by the authors, presented at the AIAA Scitech 2024 Forum [11].

In this paper, we present a combined finite element and analytical approach to evaluate and predict the SSTM's properties, with a focus on designing the boom to solar sail system requirements. Section III includes a brief review of Phase I SSTM design and testing, and discusses the composite layup configuration and changes for the Phase II boom cross-section. In Section IV, we use a combination of finite element simulations and analytical models to characterize the boom's stiffness and buckling behavior in terms of geometric design variables. This analysis is used in Section V to evaluate the mass efficiency and performance of potential boom designs, as well as the scalability of the SSTM architecture. Section VI summarizes our findings and discusses plans for future research.

III. Boom Design

A. Previous boom design and need for improvement

The initial Phase I SSTM design, shown in Fig. 1, is similar to the Trussed TCTM [10], using the same cross-section and design principles while reducing weight. It is essentially a flattenable rolling tape-spring boom where the longerons and battens were offset to enable more compact flattening and rolling. It consists of six curved longerons, connected through flat battens. Two flanges extend on the sides. In contrast with open cross-section booms, SSTM is inherently high in torsional stiffness due to its closed cross section. Because of this, and the lower torsional stiffness requirement of long booms, diagonal elements are omitted to save mass. The remaining longeron and batten tape-springs form a frame that remains stiff in shear and torsion.

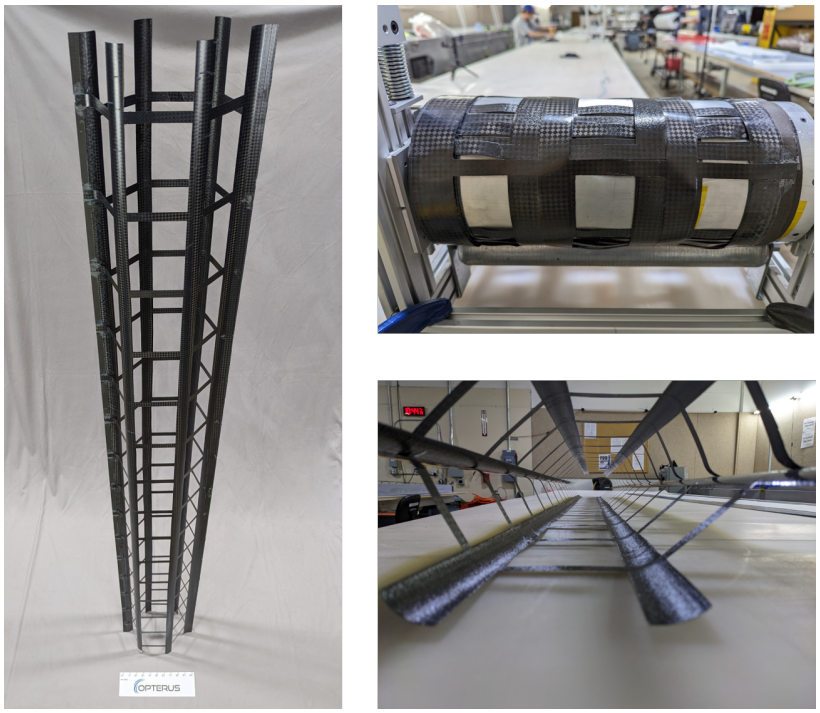

Fig. 1 The Phase I SSTM boom in deployed and rolled configurations.

All elements in the boom are built using High Strain Composites [12]. Figure 2 identifies all regions though color. All layups are a combination of ultra-thin unidirectional and plain-weave laminas, all with intermediate modulus fibers, with the stacking sequence designed based on the specific role of each element. The longerons run continuously through the structure and provide axial stiffness. Battens run perpendicular to the longerons and function to improve hoop stiffness and help maintain the cross-sectional shape to keep the longerons in proper position. They also increase the torsional stiffness. The flanges extend on the sides and help consolidate the structure and connect the battens and longerons on the top and bottom halves of the mast.

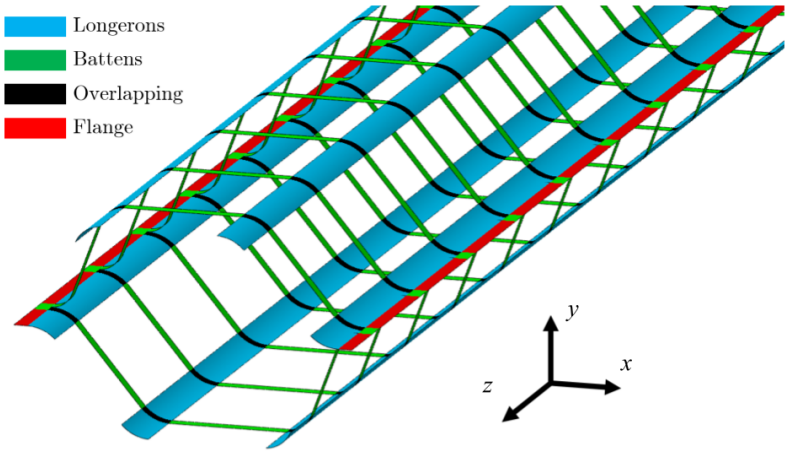

Fig. 2 Definition of Regions of the SSTM Boom.

Two prototypes with the same length (72 inches, 1.83 m), 15 battens, and different width of longerons and battens were built and tested under compression and bending, see Fig. 3. The results showed that the buckling initiates in the

longerons with lowest curvature, which are a result of using a non-symmetric cross section so that the longerons do not align when the mast is rolled and stowed. One of the goals of the new design is to achieve a new cross section in which all longerons have the same radius of curvature.

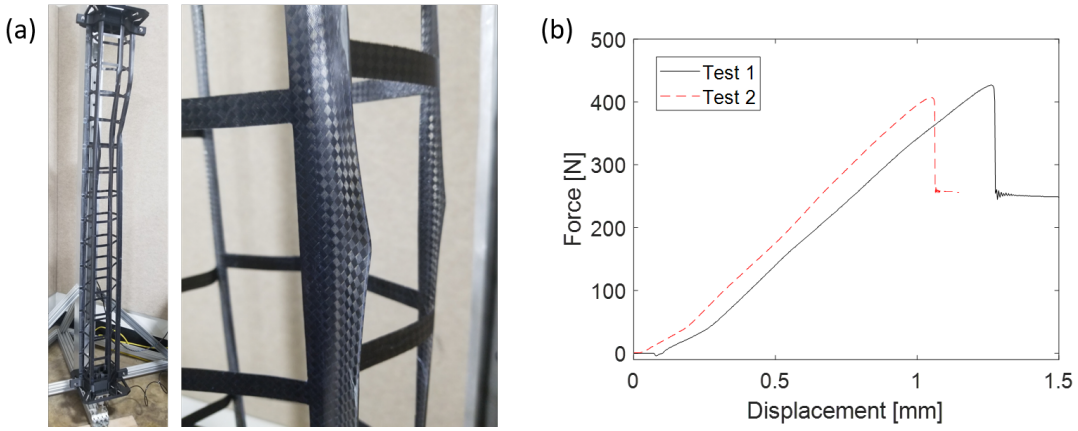

Fig. 3 (a) Pictures of the buckling on the boom, showing buckling of a longeron extending over approximately six bays. (b) Results of two tests for axial compression on prototype 1.

B. Phase II Boom Design

The new mast is different only in its cross section, which is shown in Figure 4. The new cross section is skewed (*i.e.*, the top and bottom battens are not parallel to the midline) to achieve the same radius curvature, R, in all longerons. The cross-section skewness of also allows the longerons to offset while flattened, which helps reduce volume and material strain while stowed. One of the main goals of the present study is to rationalize the effect of scaling the size of the cross-section, while keeping other geometry parameters constant. The dimensions of the cross-section will be described by the radius of the longerons, which can then be compared to their width to understand the relationship between longeron curvature and slenderness. While the Phase I SSTM prototypes were under 2 m in length, we aim to manufacture and test a 27 m Phase II boom prototype in future work.

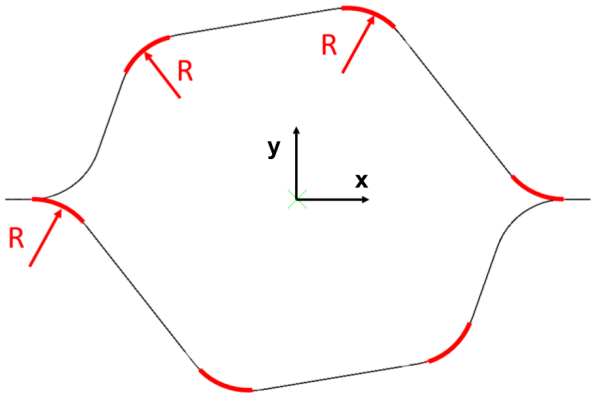

Fig. 4 Image of the new cross section, with the longerons highlighted in red. The design is skewed to achieve same curvature in all longerons.

C. Laminate Properties

Ultra-thin, high-strain, intermediate-modulus carbon fiber composites are used for all elements of the SSTM due to their high stiffness to mass ratio, and ability to withstand high strains when the boom is folded [12, 13]. Layups consist of both uni-directional (UD) and plain-weave (PW) laminas. After some simulations to compare the performance of different layups, a nominal symmetric layup of two UD laminas between two PW laminas is used for both the longerons and battens. Reducing the total number of plies below four leads to drastically reduced stiffness, particularly in torsion. Initial linear finite element analyses found that increasing the number of longeron plies improved stiffness marginally, but with a large weight gain. Increasing the number of plies in the battens did not provide a notable improvement in stiffness. Nonlinear Riks finite element results also suggest that increasing the number of PW plies can lead to very low first buckling modes, with long stable postbuckling period. The orientation of the PW plies was also evaluated, and a PW orientation of ±45° with respect to the mast's main axis was found to provide marginally higher stiffness than 0/90° orientation.

IV. Boom Analysis

We have explored the design space for the SSTM using finite element (FE) simulations under the different expected loading conditions, with an emphasis on failure due to buckling. Finite element data and observations are then used to develop analytical models for boom properties in terms of design variables. This both reduces computational time, and develop a deeper understand the underlying mechanisms behind the response of the structure.

All FE simulations are performed using the commercial finite element package Abaqus, using quadrilateral reduced shell (S4R) elements. Composite laminate layups are modeled using homogenized properties for each ply. This work relies primarily on linear response and linear eigenbuckling analyses, with some nonlinear Riks analyses used to check for the effect of geometric nonlinearity. The Abaqus finite element model is built using a Python script, such that varying combinations of geometric design variables can be explored. In particular, this analysis focuses on characterizing the boom in terms of the cross-section scale factor (Sc), longeron width (W_l), batten width (W_b) and number of battens (Nb). Note that the radius of curvature of the longerons scales with the cross-section, while the longeron width scales independently, as long as they can fit within the curved regions in the cross-section. A scaling factor of Sc =1 corresponds to a flange-to-flange diameter of 0.2 m. In this section, we aim to understand the mechanics, and perform simulations varying the parameters with respect to a small set of nominal designs, which are similar to the boom designs used in Phase I of this study. A more thorough exploration of the design space will be presented in Section V.

The loading conditions considered in this study are compression, bending around the y-axis, and torsion. In all cases, we will compare the effect that changes in geometry have not only on stiffness and strength, but also on performance metrics often used to characterize the performance of deployable masts [14].

A. Axial Compression

1. Axial Loading Conditions

Axial compression is imparted on the mast by sail tension through cables. The tension vector is oriented at an angle β from the boom, which depends on the mission phase, temperature, and the sail's angle and distance relative to the sun (or other light source) [15]. This loading case can be modeled as a force vector which intersects the vertical plane at a characteristic length, C, from the tip of the boom, as illustrated in Fig. 5 [16].

For the truss-like SSTM boom design, buckling is the expected failure mode under axial loading. For a load vector through a fixed point, the effective length, λL depends on the ratio, C/L, between the characteristic length, C and the boom length, L [15]. The value of λL can be determined by solving the following equation [16]:

$$\tan(\lambda L) = \lambda L(1 - C/L) \tag{1}$$

and the first critical buckling load, P_{cr} is given by:

$$\lambda = \sqrt{\frac{P_{cr}}{EI}} \tag{2}$$

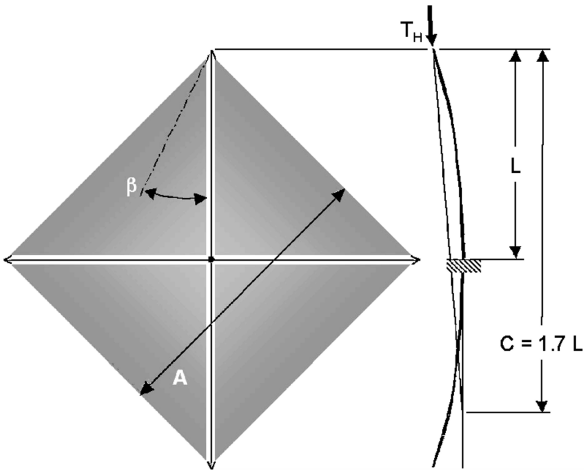

Fig. 5 Sail tension vector at an angle β from the boom, and the resultant axial force vector through a fixed point at a length C from the tip of the boom [15].

where EI is the boom's bending stiffness [16].

2. Euler-Bernoulli and Timoshenko Beam Models

Equation (2) for the axial critical buckling load relies on the assumption that the SSTM behaves as an Euler-Bernoulli beam, in which the cross section remains perpendicular to the neutral axis [16]. However, Abaqus FE simulations of the SSTM boom in bending reveals significant shear deformation and rotation of the cross-section with respect to the neutral axis, as illustrated in Fig. 5(b). This behavior is attributed to truss-like nature of the SSTM architecture, and contradicts Euler-Bernoulli beam assumptions. Unlike the Euler-Bernoulli beam model, the Timoshenko beam model [17] relaxes the constraints on shear deformation as shown in Fig. 6(a). Furthermore, the sail tension loading vector has a shear as well as an axial component, which may exasperate differences between the Euler-Bernoulli and Timoshenko beam models.

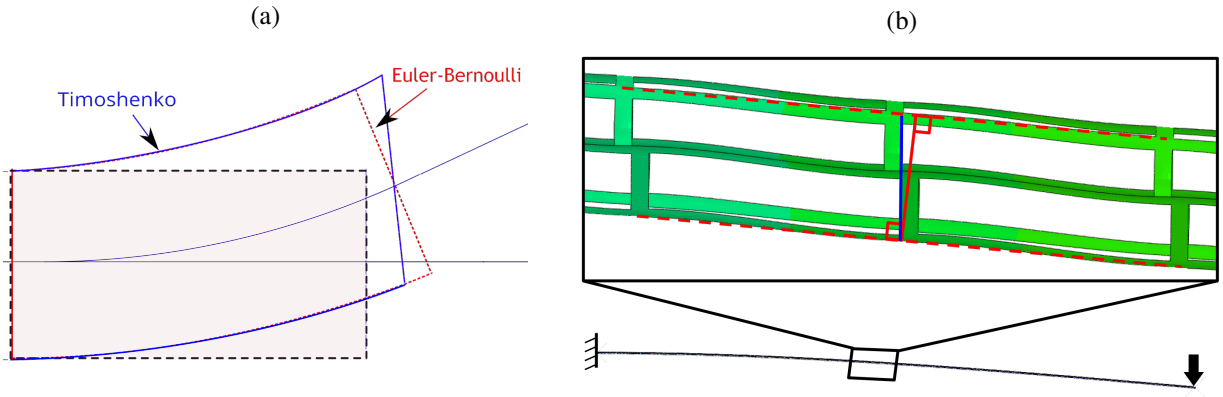

Fig. 6 (a) Schematics for the Euler-Bernoulli and Timoshenko beam models, and (b) shear deformation visible in the SSTM cross-section during cantilever bending

The axial buckling critical load for a Timoshenko beam takes the form [18]:

$$P_{cr,\,Timoshenko} = \frac{P_{cr,\,Euler}}{1 + \pi^2 \phi / b} \tag{3}$$

where b is an additional constant which depends on boundary conditions. The dimensionless parameter ϕ depends on the shear compliance of the beam, and is defined as:

$$\phi = \frac{12EI}{(\kappa_s GA)L^2} \tag{4}$$

where GA is the beam's shear rigidity, and κ_s is the shear correction coefficient. While closed-form solutions exist to estimate $\kappa_s GA$ for homogeneous beam sections, such as a rectangular or circular beam, estimating $\kappa_s GA$ for the SSTM is more complex. Here, we take advantage of the lack of shear forces in a beam under pure bending conditions. Bending stiffness can be estimated using simulations of the SSTM boom in pure bending, and the $\kappa_s GA$ term can be back-calculated from the boom's tip deflection in simulations of cantilever bending, where we expect the same bending stiffness but also the effect of the shear compliance.

3. Global and Local Axial Buckling Modes

Another important consideration for axial compression is whether the resulting buckling modes are local or global. Global buckling modes are those expected for a slender beam, and can generally be predicted using classical beam theory as discussed above. Local modes, by contrast, may involve only some components of the overall structure, and cannot be predicted by modeling the SSTM as a homogenized beam. Local modes may be periodic along the length of the boom, or localized to a single element, for example a longeron. Linear eigenbuckling simulations conducted on the SSTM show that for short beams, the lowest buckling load is associated with localized modes, while for long beams global modes dominate. For long beams, however, higher-order mode shapes show a combination of both global and local buckling modes, as illustrated in Fig. 7. A comparison of the local periodic mode characteristic of short SSTM architectures, and the local components of combined high-order modes for long beams reveals qualitative similarities. For a given mast design, the load required to initiate local buckling is independent of boom length.

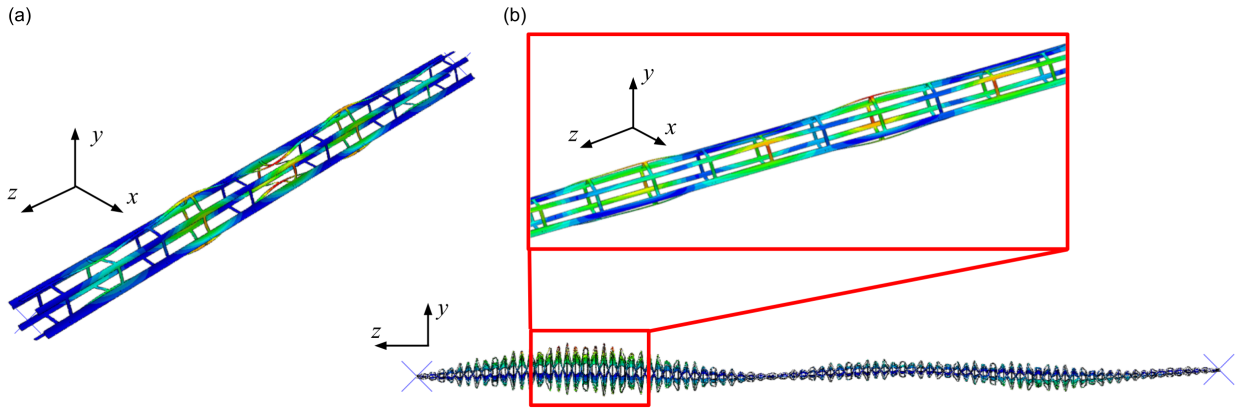

Fig. 7 (a) Local axial buckling mode shape for a 1.524 m length boom compared to (b) a combined local and global buckling mode for a 27 m boom.

Global axial mode shapes appear qualitatively similar to the well-known shapes expected for Euler-Bernoulli buckling, particularly for the first mode. As an example, mode shapes for fixed-free boundary conditions from a linear eigenbuckling analysis in Abaqus are shown in Fig. 8. Expected mode shapes for an Euler-Bernoulli beam are plotted next to the mode shapes from Abaqus for comparison. Due to the anisotropy of the SSTM, bending stiffness is higher about the y-axis than about the x-axis. The lowest global buckling mode is therefore driven by the bending stiffness about the x-axis, EI_X, while higher mode shapes can depend on EI_Y.

4. Testing the Validity of the Euler-Bernoulli and Timoshenko Beam Models for Estimating Axial Buckling Loads

In order to test the applicability of the Euler-Bernoulli and Timoshenko beam models, axial buckling finite element simulations were performed for a SSTM of various lengths and boundary conditions. While the SSTM's bending stiffness, EI, is independent of boom length, the value of $\kappa_s GA$ does vary with length, due to the effect of boundary

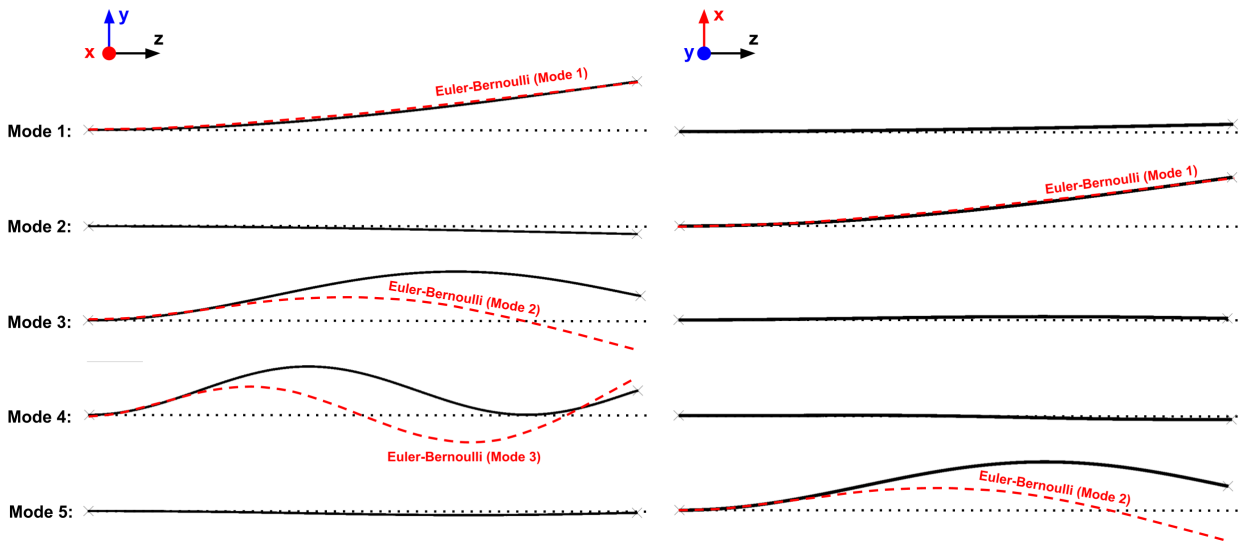

Fig. 8 Global buckling mode shapes for the SSTM boom under axial compression with fixed-free boundary conditions. Mode shapes from finite element analysis (black) are overlayed with exact solutions for mode shapes expected of an Euler-Bernoulli beam (dashed red). Each mode shape is displayed from two perspectives, facing the y-z and x-z planes.

conditions. We therefore compare two values of $\kappa_s GA$, one based on a 1.524 m boom, referred to as the "short" beam model, while the second is based on a 27 m boom, referred to as the "long" beam model.

Figure 9 shows FE data plotted against expected axial buckling loads according to the Euler-Bernoulli and Timoshenko beam models, as a function of the boom length. Figure 9(a) shows results for fixed-fixed boundary conditions, while Fig. 9(b) shows results for fixed-free boundary conditions.

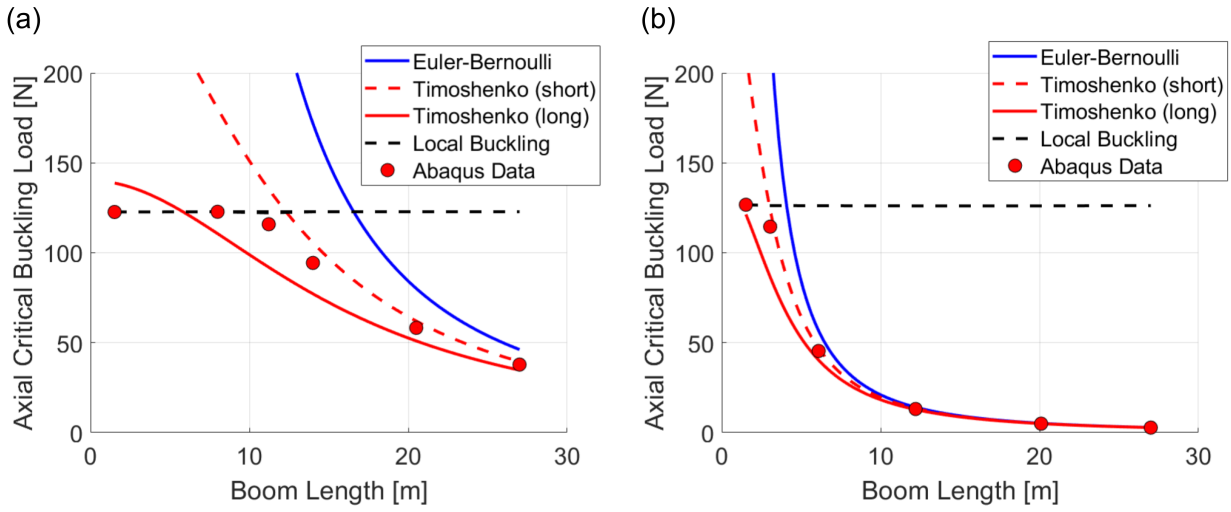

Fig. 9 Comparison of the Euler-Bernoulli and Timoshenko beam buckling models plotted against Abaqus FE Results for (a) fixed-fixed boundary conditions and (b) fixed-free boundary conditions.

Several key observations can be made from Fig. 9. First, the FE results for axial buckling loads fall between the predictions from the two Timoshenko models, with the "short" 1.524 m model providing a closer approximation. Second, the local buckling load is independent of boom length. For fixed-fixed boundary conditions, the transition from local to

global buckling occurs at approximately 11 m, while for fixed-free conditions global buckling begins to dominate at just $L = 3$ m. It is also clear that, especially for fixed-fixed conditions, the Euler-Bernoulli model fails to accurately predict the local-global transition. Finally, there is a larger gap between the Euler-Bernoulli and Timoshenko models for fixed-fixed boundary conditions compared to fixed-free conditions, which can be interpreted as a result of the different effective lengths between both boundary conditions. Our results suggest that, for the 27 m boom prototype which is the goal of this project, the Euler-Bernoulli model provides a reasonable estimate for axial critical load under fixed-free boundary conditions.

From Murphey, [15], we anticipate characteristic length ratio up to $C/L \approx 1.7$ due to solar sail tension. While neither fixed-fixed nor fixed-free boundary conditions accurately reflect loading due to sail tension, fixed-free conditions serve as a conservative estimate for critical buckling load. Since finite element results closely match predictions using the Euler-Bernoulli beam model with fixed-fixed conditions, we conclude that the Euler-Bernoulli model provides a reasonable estimate of the boom's buckling response at a length of 27 m.

Modeling the sail tension loading vector on a detailed FE model of the boom is computationally expensive, and still may not provide useful results unless the entire sail-boom system is included. Instead, system-level model with the boom represented as a simple Euler-Bernoulli beam is used. From the system-level model, we can define minimum bending stiffness for the boom in order to avoid axial buckling.

B. Bending Stiffness and Critical Buckling Moment

1. Bending Stiffness

Bending stiffness influences not only the axial buckling behavior of the boom, but tip deflection in bending as well. Estimating and understanding the bending stiffness for the SSM is therefore a critical design step. In order to reduce computational time on large FE simulations, we aim to develop an analytical model for SSTM bending stiffness in terms of the boom design parameters: cross-section scale factor (Sc), longeron width (W_l), batten width (W_b) and number of battens (Nb).

To simplify the analysis, we assume that the boom's bending stiffness is carried by the longerons and flanges, with negligible contributions from the battens. It should be noted that this also neglects the region where the longerons and battens overlap, which probably have a larger influence. We then apply the parallel axis theorem to develop expressions for the boom's bending stiffness about the x and y axes. Because each longeron is a thin open curved section, the second moment of area of each individual longeron is several orders of magnitude smaller than the second moment of area of the entire boom, and can be neglected. Bending stiffness is then driven by the area of each longeron and flange multiplied by the square of their distance from the bending axis. For bending about the x-axis, the longeron area scales linearly with longeron width, W_l, and the distance from the x-axis scales linearly with the cross-section scaling factor, Sc. The bending stiffness for bending about the x-axis can therefore be written as:

$$EI_X \approx C \cdot W_l Sc^2 \tag{5}$$

where the constant C depends on the geometry of the cross-section and the properties of the laminate. For bending about the y-axis, the flanges are also taken into consideration. Both the flange width and distance between the flanges and the y-axis scale linearly with the cross-section scaling factor, Sc. Therefore, the expression for bending stiffness about the y-axis takes the form:

$$EI_Y \approx C_1 \cdot W_l Sc^2 + C_2 \cdot Sc^3 \tag{6}$$

where $C1$ and $C2$ are again constants that capture the effect of the specific cross-section geometry and the material properties. The constants in equations Eq. (5) and Eq. (6) are estimated by fitting the analytical expressions to finite element results for the boom's bending stiffness. This is achieved by running a linear analysis with the boom under pure bending. The tip deflection angle, θ, is then used to estimate the bending stiffness using the well-known relationship for pure bending:

$$EI = \frac{ML}{2\theta} \tag{7}$$

where M is the moment applied to the boom in pure bending, and L is the boom length. After using finite element data to calibrate the analytical expressions at a range of longeron width and cross-section scaling factor values, we arrive at the following expressions:

$$EI_X \approx 3.36e5 \cdot W_l Sc^2 \tag{8}$$

$$EI_Y \approx 4.5e5 \cdot W_l Sc^2 + 2.1e3 \cdot Sc^3 \tag{9}$$

in which it is assumed that W_l is expressed in meters and EI in Nm^2. From the equations above, it is clear that the bending stiffness about the y-axis is larger than the bending stiffness about the x-axis. This anisotropy is not surprising, given the SSTM cross-section shape. The ratio between EI_Y and EI_X can be estimated by dividing Eq. (9) by Eq. (8), and neglecting the small contribution from flanges, giving a ratio of $\frac{EI_Y}{EI_X} \approx 1.34$.

Figure 10 provide a visual comparison of the analytical expressions for bending stiffness against Abaqus FE results. Each plot shows the dependency of bending stiffness on each of the four boom design parameters. These results show that our simplified model provides a reasonable approximation of the FE results, with drastically less computational time. Furthermore, the observation that bending stiffness is independent of boom length, and can be closely approximated using only the longeron width and cross-section scale serves to simplify the design process.

2. Buckling Critical Moments in Bending

A system-level model of the boom and sail can provide a maximum expected bending moment on the boom. The boom can then be designed such that the critical buckling moment due to bending is larger than the maximum expected moment. We aim to develop an analytical expression for the critical buckling moment using the same approach as we did with bending stiffness. Observations of FE eigenvalue buckling results in preliminary designs revealed that local buckling modes dominate in bending. In particular, the longeron furthest from the neutral axis exhibits periodic local buckling over several bays closest to the clamped root, as shown in Fig. 11. Eigen buckling simulations also indicate that the critical buckling moment is the same for both cantilever and pure bending cases. The first mode shape for pure bending is also characterized by a single periodic longeron buckle, but is not limited to the clamped end because the moment is constant along the boom. The first critical buckling moment is also observed to be constant with respect to boom length for 1.524 m$< L <$ 27 m.

We now aim to develop and analytical closed form expression for the bending moment at which the longeron furthest from the bending axis buckles. For a beam under pure bending with an applied moment M, compressive strain at a distance y from the bending axis is given by:

$$\epsilon = \frac{-My}{(EI)_{boom}} \tag{10}$$

where $(EI)_{boom}$ is the boom's bending stiffness. To approximate the axial compressive force on a single longeron, the strain in Eq. (10) is multiplied by the axial stiffness of the longeron, which in our case can be also be approximated as $\frac{1}{6}(EA)_{boom}$. At the moment of buckling, this compressive force is equal to the compressive force required to buckle the longeron furthest from the bending axis. The axial buckling load for a single longeron using Euler-Bernoulli beam theory is:

$$P_{cr} \approx \frac{(EI)_l}{k^2 l^2} \tag{11}$$

where $(EI)_l$ is the longeron bending stiffness, l is the longeron length, and the k parameter is determined by boundary

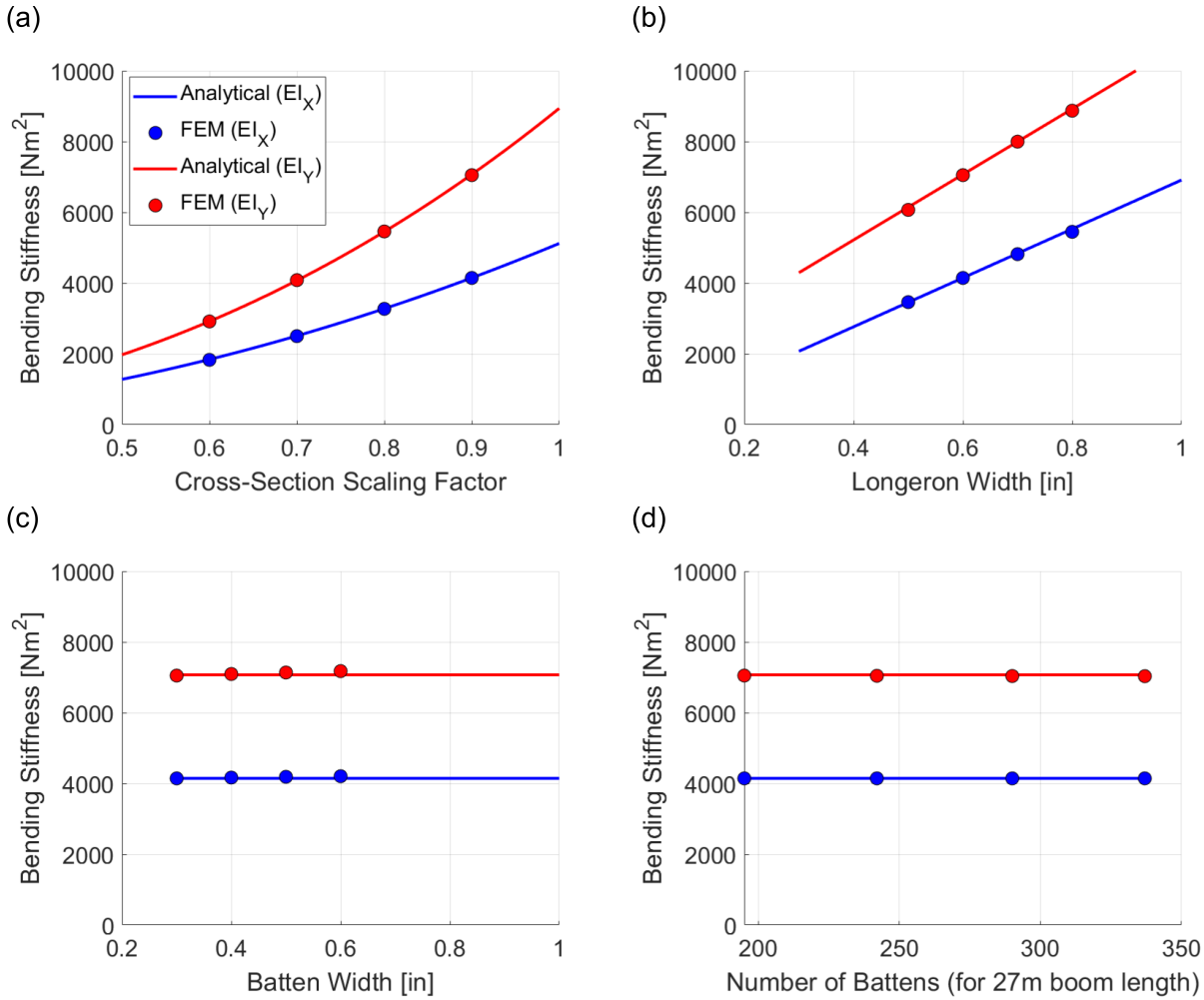

Fig. 10 Bending stiffness from Abaqus FE simulations compared to analytical models for EI_X and EI_Y for varying (a) cross-section scale, (b) longeron width, (c) batten Width, and (d) number of battens.

conditions. Setting the resulting compressive force from Eq. (10) equal to Eq. (11) and rearranging for the critical buckling moment results in the following expression:

$$M_{cr} \approx 6\pi^2 \cdot \frac{1}{k^2} \frac{(EI)_{boom}(EI)_l}{(EA)_{boom} l^2 y} \tag{12}$$

Next, we can approximate each term in Eq. (12) using boom design variables. The distance of the furthest longeron from the bending axis, y, scales linearly with the cross-section scaling factor, Sc. The bending stiffness of the entire boom, $(EI)_{boom}$, is approximated analytically by Eq. (8) and Eq. (9). The axial stiffness of the boom, $(EA)_{boom}$ can be similarly approximated by assuming the axial stiffness is dominated by the longerons. Therefore, the boom axial stiffness scales linearly with longeron width, W_l. The bending stiffness of each longeron can be estimated using the expression for the second moment of area for a thin open section from [19]:

$$(EI)_l \approx r^3 t\alpha \left(\frac{1}{2} \frac{\sin 2\alpha}{\alpha} + 1 - 2\frac{\sin^2 \alpha}{\alpha^2} \right) \tag{13}$$

where t is the longeron thickness, and α and r are half the subtended angle and radius of curvature of the shallow-curved longeron, respectively (see Fig. 12). Because the radius of curvature of the longerons scales with the cross-section scaling factor, Sc, and the longeron width, W_l, scales independently, the half subtended angle α is proportional

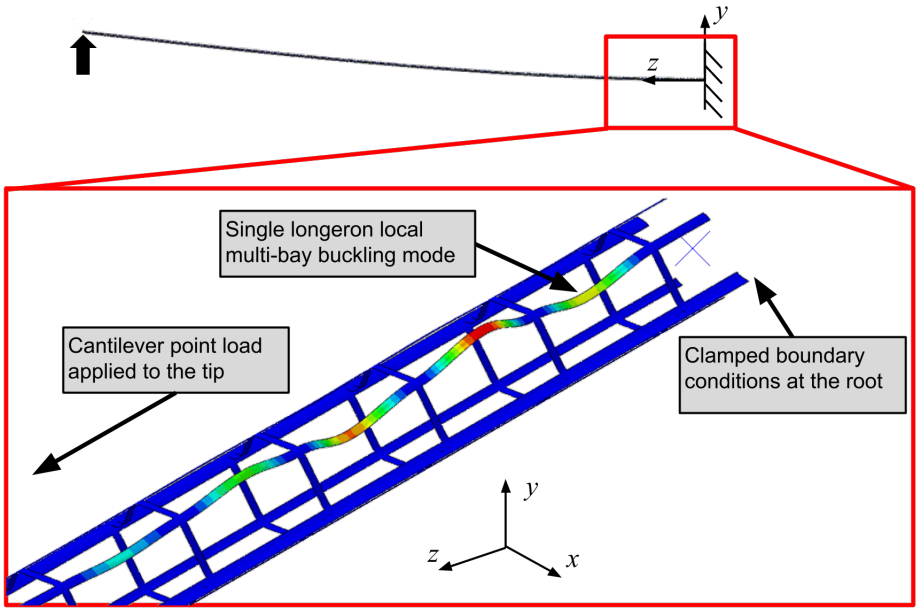

Fig. 11 A typical buckling mode shape for the SSTM in cantilever bending about the x-axis, localized to a single longeron near the clamped root of the boom.

to the ratio between longeron width and the cross-section scaling factor, $\frac{W_l}{Sc}$. To simplify the model, the term, $f(\alpha) = \left(\frac{1}{2}\frac{\sin 2\alpha}{\alpha} + 1 - 2\frac{\sin^2 \alpha}{\alpha^2}\right)$ can be approximated closely within the expected range of our design variables as $f(\alpha) \approx g(W_l/Sc) = 4e3 \cdot \left(\frac{W_l}{Sc}\right)^{3.93}$.

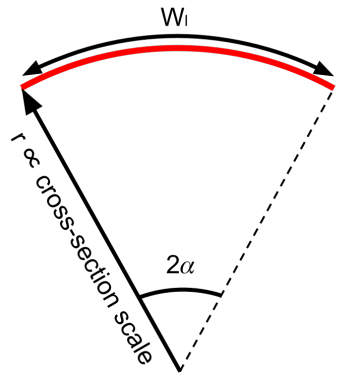

Fig. 12 A longeron cross-section shown in red, defined by it's radius, r, and half subtended angle, α.

The longeron length variable, l, in equation Eq. (12), is not immediately obvious, due to the fact that each longeron is not independent, but is connected to the rest of the boom structure via the battens. As an approximation, we will use the bay length, or length between battens, such that:

$$l^2 \approx (L/Nb - W_b)^2 \tag{14}$$

where Nb is the total number of battens, L is the total boom length, and W_b is the width of each batten. For classical Euler buckling, the parameter k^2 depends on the boundary conditions. For the case of a single longeron buckling, the boundary conditions are unclear. However, observations of the buckling modes in bending reveal that longeron buckling

occurs periodically over the span of one or more battens. If the buckling mode is periodic over B bays, then the effective length is $kL = BL$. While we do not provide an explicit expression for k in terms of design variables, we can make informed guesses as to which design variables increase or decrease k. We assume that increasing the batten width, or increasing the number of battens per unit length will both increase k, while increasing the cross-section scaling factor may reduce k. Substituting each term in Eq. (12) with approximations using only the design variables, we arrive at the following expression for critical buckling moment:

$$M_{cr} \approx C \cdot \frac{1}{k^2(W_b, Nb, Sc)} \cdot \frac{W_l^{4.93} Sc^{-0.93}}{(L/Nb - W_b)^2} \tag{15}$$

where C is a constant, and $k(W_b, Nb, Sc)$ is a function of batten width, number of battens, and cross-section scale factor. Due to uncertainties introduced by the k term in particular, we modified to model such that each design variable is raised to some exponent. Exponent values were then calculated by minimizing the sum of squared errors between the analytical model and Abaqus data for critical buckling moment, for a wide range of values of the design variables. The result are two analytical expressions for the critical buckling moment about the x-axis and y-axis respectively:

$$M_{cr,X} \approx 8.84e5 \cdot Sc^{-1.22} \cdot W_l^{2.90} \cdot W_b^{0.36} \cdot (L/Nb)^{-1.04} \tag{16}$$

$$M_{cr,Y} \approx 2.02e5 \cdot Sc^{-0.78} \cdot W_l^{2.11} \cdot W_b^{0.60} \cdot (L/Nb)^{-1.04} \tag{17}$$

Several differences between Eq. (15), Eq. (16) and Eq. (17) are noteworthy. First, the cross-section scale factor exponent differs significantly between Eq. (16) and Eq. (17). This difference can be partially explained by the contribution of the flange, which scales linearly with the cross-section and only contributes to bending about the y-axis. The larger negative exponent on the cross-section scale term in Eq. (16) compared to the prediction from Eq. (15) indicates that the cross-section scale does have some small influence on the k^2 boundary condition term. Another notable difference is that the exponent for longeron width is smaller in both Eq. (16) and Eq. (17) than predicted by Eq. (15). A potential explanation for this discrepancy could be a more complex interaction between the longerons, flanges and battens which is not captured by our analysis. Longeron width also appears to have a larger influence on the critical buckling moment for bending about the x-axis compared to bending about the y-axis. By contrast, batten width has a stronger influence on bending critical moment for bending about the y-axis. In general, the bending critical moment increases with batten width. As anticipated, the boom length per batten, or bay length, is inversely proportional to the bending critical moment.

The analytical models for bending critical moment are compared in Fig. 13 to FE data collected using Abaqus. For most cases, the 1st buckling mode is characterized by periodic local longeron buckling. However, for some cases involving small cross-section scales, or large numbers of battens, the lowest mode is global. Because the closed form approximation is based on the assumption of periodic local longeron buckling, global modes are not predicted. When local buckling is the lowest mode, the model provides a reasonable estimate within the design variable ranges considered.

C. Cantilever Bending and Tip Deflection

Tension applied orthogonally to the tip of the SSTM due to solar pressure and subsequent sail bellowing can be modeled as cantilever bending, with the boom fixed at the root and free at the tip. The amount of expected boom deflection at the tip is the primary design concern. Additionally, we examine out-of-plane bending due to the anisotropy of the SSTM cross-section. Under the Timoshenko beam model, tip deflection for a cantilever beam with tip load P is given by [17]:

$$\delta_{tip} = \frac{PL^3}{3EI} + \frac{PL}{\kappa_s GA}. \tag{18}$$

The $\frac{PL^3}{3EI}$ term defines tip deflection for a Euler-Bernoulli beam, and thus the two beam models converge when $\frac{3EI}{L^2\kappa_s GA} << 1$ (Ref.[18]). Tip deflection for the SSTM is calculated using a linear Abaqus FE simulation with a small tip load. However, it is unclear from a cantilever analysis how much the boom deflection is influenced by bending stiffness, or the Timoshenko term $\kappa_s GA$. Because pure bending conditions should involve no shear forces, the

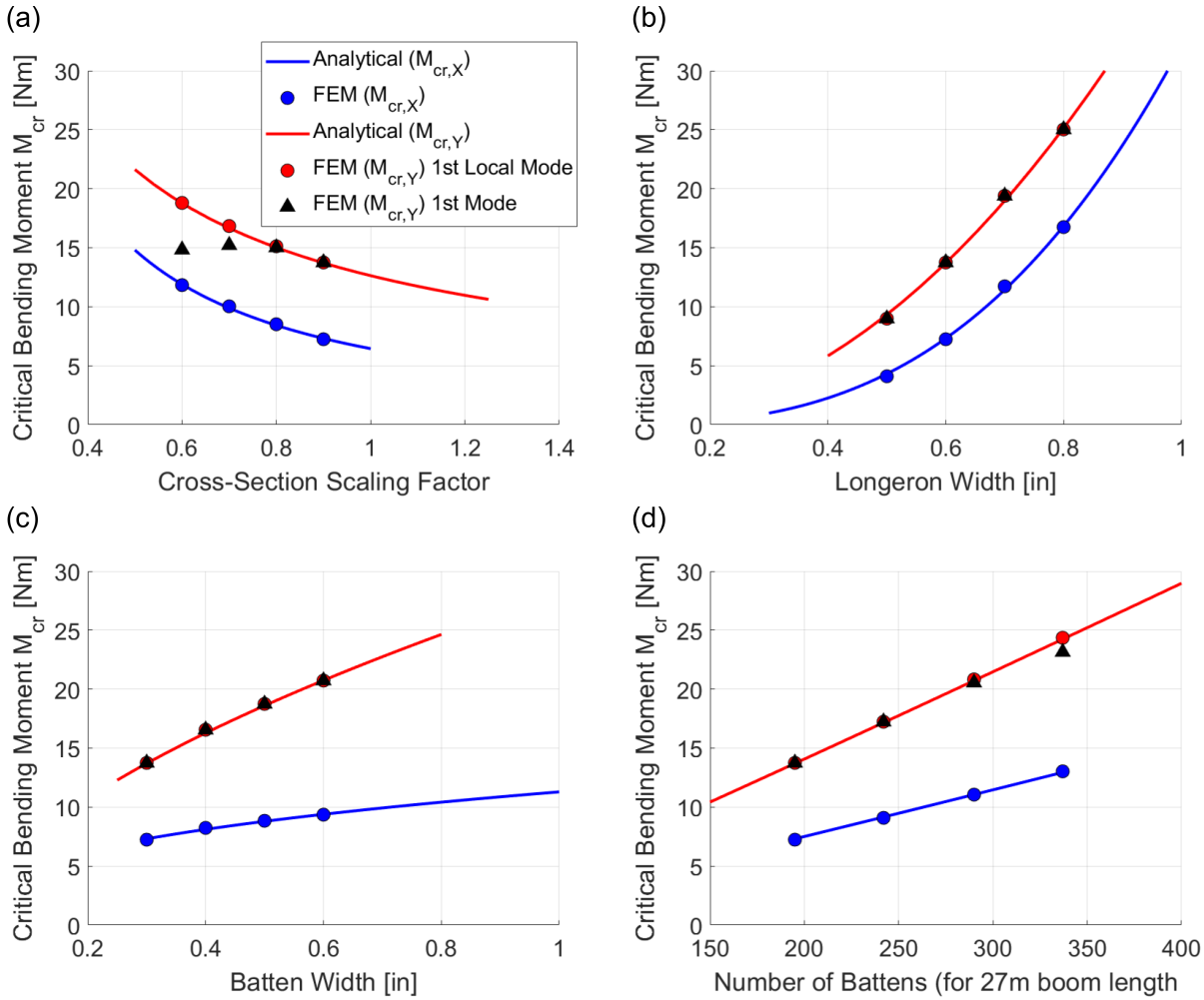

Fig. 13 Bending critical buckling moment from Abaqus FE simulations compared to analytical models for $M_{cr,X}$ and $M_{cr,Y}$ for varying (a) cross-section scale, (b) longeron width, (c) batten Width, and (d) number of battens.

pure bending response is independent of $\kappa_s GA$. Pure bending FE simulations in Abaqus are therefore used to evaluate the bending stiffness of a given SSTM design, and the $\kappa_s GA$ can be back-calculated from the cantilever tip deflection.

Some out-of-plane deflection is also expected for cantilever bending due to the anisotropy of the SSTM cross-section, with $EI_Y/EI_X \approx 1.34$. Both linear and nonlinear FE simulations showed that for bending about the y-axis, the ratio between tip deflection in the y-axis and x-axis is approximately $1/8$. While the out-of-plane deflection is relatively small, it could be significant with regards to the system-level boom-sail interaction.

D. Torsion

1. Torsional Stiffness

A third important loading condition to consider is torsion caused by rotation of the deployer with respect to the mast. This can be modeled as a torque applied to the tip of the boom though sail cable tension, with the root of the boom fixed to the deployer.

Torsional stiffness, GJ, is a homogenized beam parameter that relates applied torque to the rotation angle of the

beam cross-section. While we do not have a specific requirement for the SSTM's torsional stiffness, it is important to develop an understanding of which design variables influence torsional stiffness. We therefore used linear simulations to estimate the torsional stiffness for various combinations of SSTM design variables. Figure 14 shows the influence of each of the four primary design variables on the boom's torsional stiffness. Two designs are plotted as examples to demonstrate overall trends across a wider range of design variables. Design 1, plotted in red, is representative of designs with larger cross-sections and wider battens, while Design 2 represents designs with smaller cross-sections and narrower battens.

We observe several trends from Fig. 14. First, both the batten width and number of battens appear to scale quasi-linearly with torsional stiffness , while longeron width appears to scale exponentially. This result is unsurprising, given the truss-like architecture of the SSTM. The influence of the cross-section scale on torsional stiffness, however, is less clear. For Design 2 with narrow longerons, small changes to the scale have little effect on torsional stiffness, while for Design 1 with wider longerons, increasing the scale reduces torsional stiffness. Torsional stiffness also depends on boom length, with a roughly 20% drop in torsional stiffness from a 1.524 m boom to a 27 m boom.

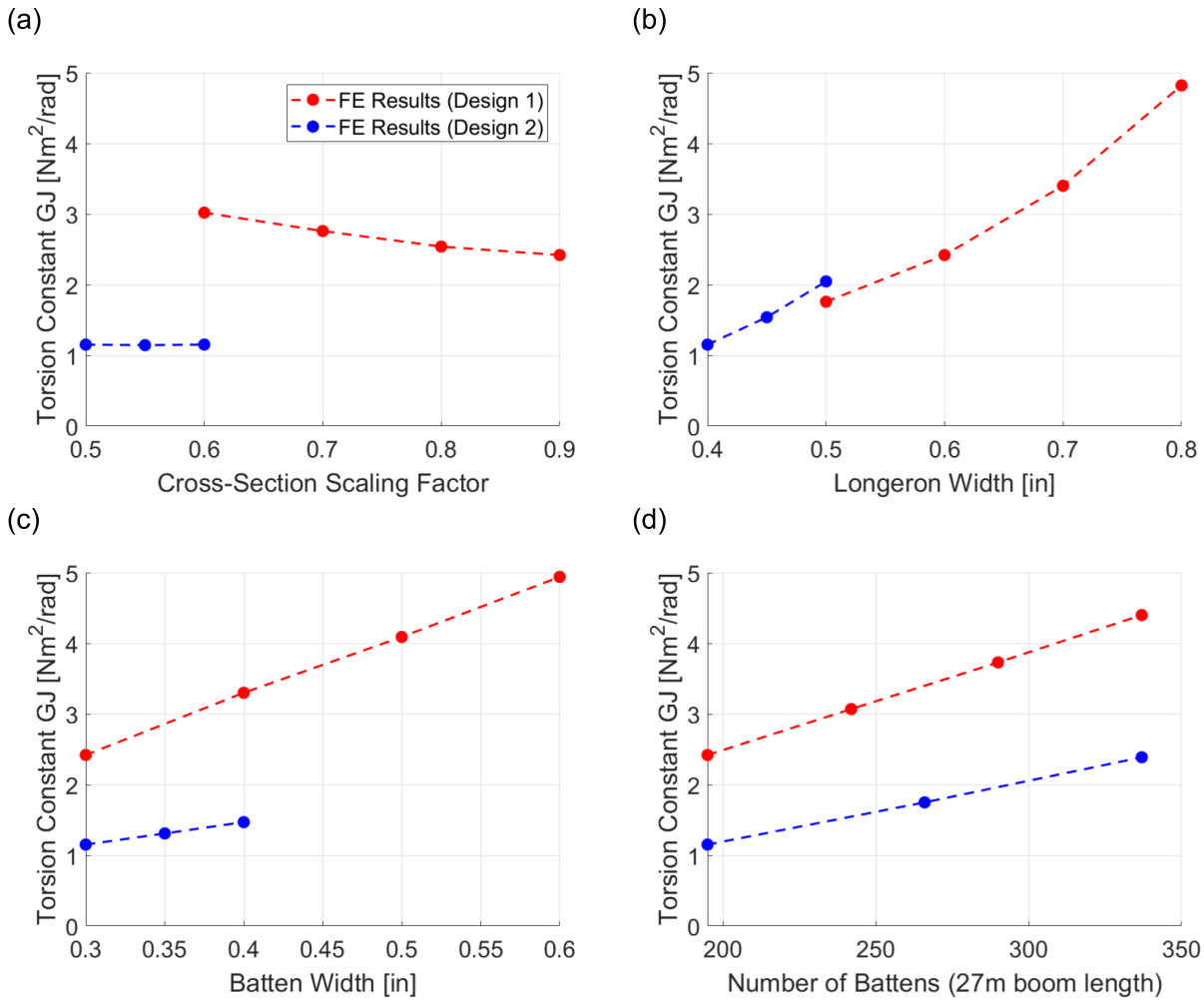

Fig. 14 Torsional stiffness from Abaqus FE simulations for varying (a) cross-section scale, (b) longeron width, (c) batten width, and (d) number of battens.

2. Buckling Moments Under Torsion

Torsion loading conditions may also lead to buckling of the SSTM structure. Linear eigenvalue buckling FE simulations are used again here to understand the influence of each design variable on the torsion buckling critical moment, with examples plotted in Fig. 15.

As was the case for torsional stiffness, the torsion buckling moment increases quasi-linearly with batten with and number of battens. Conversely, the cross-section scale is clearly inversely proportional to the torsion critical moment. The influence of longeron width is more complex, and appears not to be independent of the rest of the structure. For example, Design 1 results indicate that the torsion buckling moment decreases significantly for longeron widths less than 0.4". However, for Design 2, increasing longeron width from 0.5" to 0.8" has a less drastic impact on the buckling moment. For both designs, the increase to the buckling moment gained more longeron width diminishes as longeron width increases.

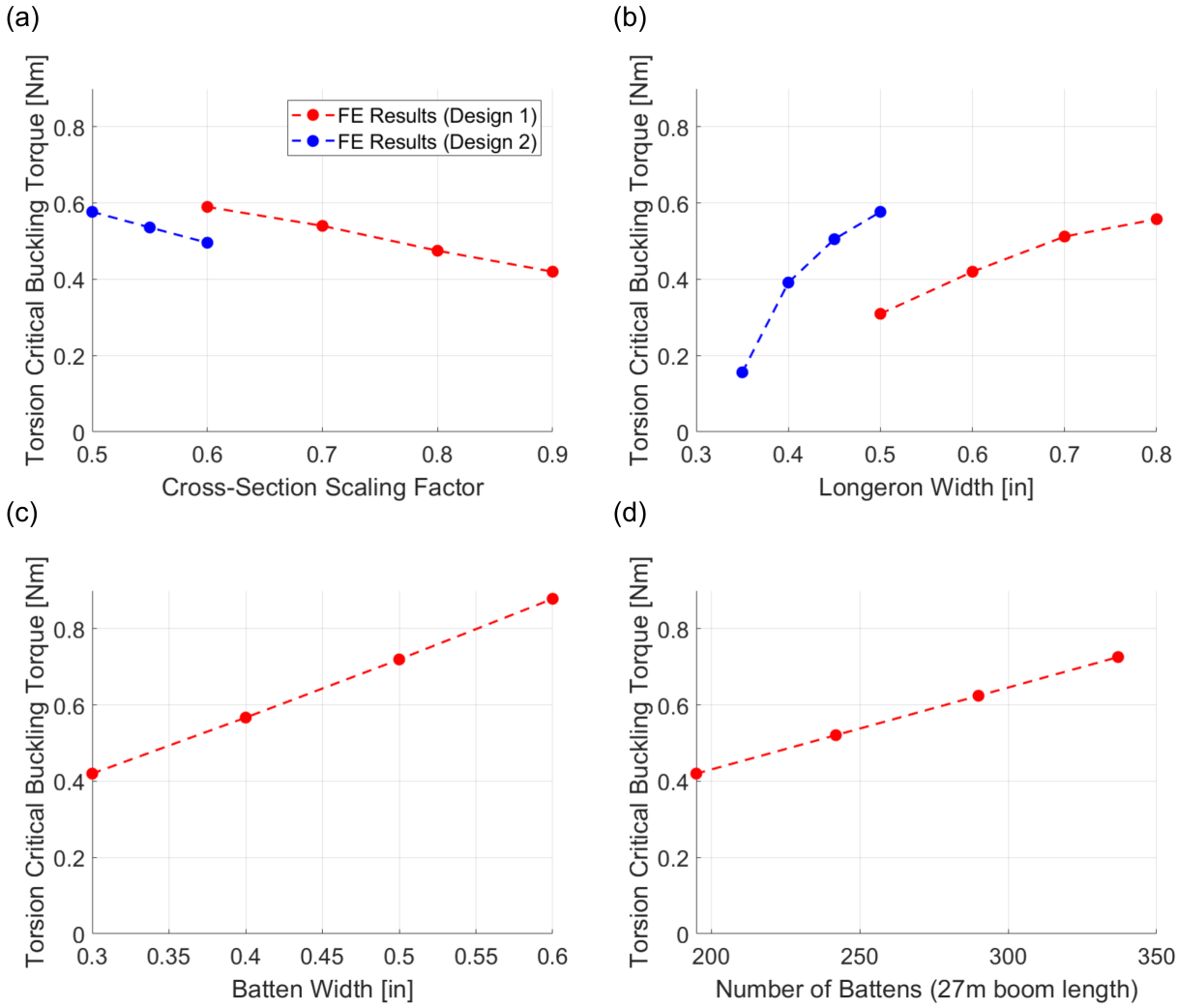

Fig. 15 Torsion critical buckling moment from Abaqus FE simulations for varying (a) cross-section scale, (b) longeron width, (c) batten Width, and (d) number of battens.

Buckling mode shapes for the SSTM under torsion involve interactions between the longerons and battens, and are more complex than axial or bending mode shapes. Mode shapes generally fall into one of two categories, either a periodic twisting mode over the entire boom, or a highly localized mode involving a single longeron near the tip where torque is applied. Examples of each type of mode shape are shown in Fig. 16.

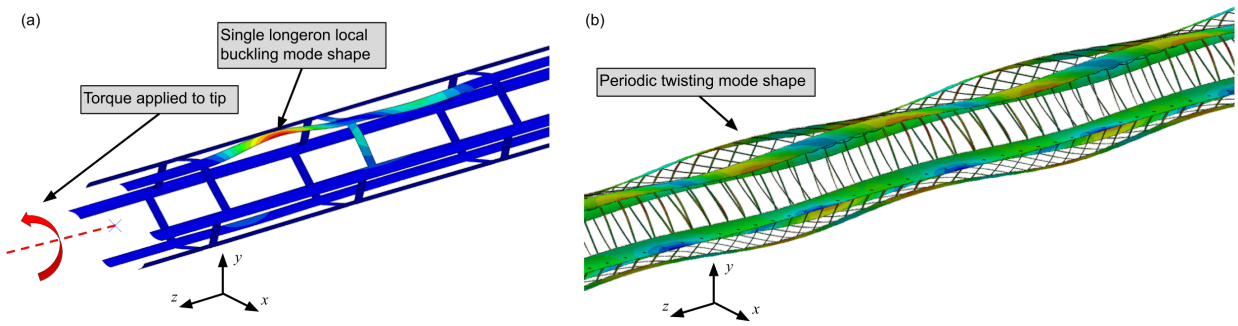

Fig. 16 Two common buckling mode shapes for the SSTM under torsion. (a) Shows the mode shape localized to a single longeron near the tip where torque is applied, and (b) shows the periodic mode characterized by global twisting.

Longeron width appears to have the largest contribution to mode shape among the SSTM design variables. For small longeron widths, roughly less than 0.4", the localized longeron mode is observed, while for longeron widths greater 0.4", the global twisting mode is most common. Critical torsion moments are significantly smaller for localized longeron modes, compared to twisting modes. This also matches the observation that torsion buckling mode drops-off sharply for longeron widths less than 0.4".

While a closed form approximation for the torsion buckling moment would serve as a useful design tool, current efforts have not yet resulted in an expression with sufficient agreement to FE results. Rather than utilizing an over-fitted, and potentially misleading, model we chose rely on the trends shown in Fig. 15 to inform design decisions. FE simulations can then be run on individual designs in order to evaluate the torsion buckling moment.

V. Mass Efficiency and Performance Results

The boom analysis in Section IV is intended to facilitate the design of an SSTM boom prototype for fabrication and testing. The finite element and analytical models for boom mechanics are used to evaluate different boom designs against design requirements. Design requirements for bending stiffness, bending critical buckling moment, tip deflection in bending, and critical torsion moment were calculated from a system-level model of the mast and sail, and are shown in Table 1.

We aimed to identify combinations of boom design variables which meet these design requirements, while minimizing boom mass per length. We also consider a bending performance metric, which can be used to compare different boom types, and is defined as:

$$\mu_B = \frac{((EI)M_{cr}^2)^{1/5}}{w} \tag{19}$$

where M_{cr} is the critical buckling moment under pure bending, EI is the bending stiffness, and w is the weight per unit length [14].

A. Constraining the Design Space and Minimizing Boom Mass

The closed form approximations for bending stiffness and critical buckling moment introduced in sections IV.B.1 and IV.B.2 are used to evaluate a large number of design variable combinations with much less computational time than FE methods. Analytical bending stiffness and bending critical moment estimates, as well as the boom's mass per length, are used to estimate the boom's bending performance using Eq. 19. Because torsion and tip deflection requirements require finite element analysis for each combination of parameters, these requirements are evaluated after first constraining the design space using bending stiffness and bending buckling requirements.

Table 1 SSTM boom design requirements

Property	Requirement
Boom length	$L = 27\,\text{m}$
Bending stiffness	$EI_Y \geq 3337\,\text{Nm}^2$
Bending critical buckling moment	$M_{\text{cr,Y}} \geq 0.26\,\text{Nm}$
Torsion critical buckling moment	$M_{\text{cr}} \geq 0.08\,\text{Nm}$
Cantilever tip deflection (at 0.26 Nm moment)	$\delta \leq 10\,\text{cm}$
Mass per unit length	$w \leq 50\,\text{g/m}$

We evaluated a wide range of design variables in order to identify boom designs which meet the requirements in Table 1. In particular, we considered cross-section scales between 0.3 and 2, longeron and batten widths from 0.25" – 1.5", and between 10 and 1000 battens. The mass per unit length and bending performance metric were calculated for each combination of design variables. To visualize the design space, designs which meet both the stiffness and bending buckling requirements are plotted in blue in Fig. 17, while those which failed one or both requirements are plotted in red. From Fig. 17, the design space is bound on the left by the bending stiffness requirement, and bound on the bottom by the bending buckling moment requirement. Our design target of $w \leq 50$ g/m further constrains the design space. It is important to note that two designs that coincidentally have the same bending performance and weight per length, and therefore are close to each other in the plot, could nevertheless differ significantly in their geometry and other performance metrics. Also, designs to the right of the orange dashed line may not meet bending stiffness requirement, although all cases to the left of this line do not meet the minimum bending stiffness requirement.

A shortlist of design candidates was then selected from within this design space, and Abaqus FE simulations were used to evaluate the torsion critical moment, and tip deflection under cantilever bending. It was found that tip deflections for these designs was always well within the design requirement of $\delta \leq 10cm$. However, torsion was revealed to be a limiting factor in terms of mass minimization. Among the shortlist of design candidates, those which did meet the torsion requirement are plotted in green, while those which did not are plotted in red. The design was then refined further. Refined designs currently under consideration are plotted as cyan triangles. An example of a refined design candidate is shown in Fig. 18, with design variables listed in Table 2. Finite element simulations were used to validate the accuracy of our analytical models for bending stiffness and bending critical moment. Bending stiffness analytical predictions matched FE results with errors between 1-2.5%, while bending critical moment predictions different from FE results by up to 14%. However, given the design requirements in Table 1, buckling in torsion appears to be the limiting factor rather than buckling in bending.

B. Evaluating the Scalability of the SSTM Boom

The analytical models for bending stiffness and critical buckling moment introduced in Sections IV.B.1 and IV.B.2 are are also used to evaluate the effect of cross-section scaling on the boom's bending performance and weight per length. Fig. 19(a) shows the effect of scaling the cross-section diameter for constant ratios between the longeron width and scale, while Fig. 19(b) illustrates the effect of changing the longeron width for a given cross-section scale. Comparing both figures reveals that while increasing the cross-section scale and longeron width both increase bending performance, increasing only the longeron width provides a larger gain in performance for a smaller gain in mass per length. Note that we assume a minimum longeron width of $W_l \geq$0.25" based on manufacturing capabilities. There is also a maximum value for the longeron width, $W_l \leq 0.9525Sc$ m, since the longerons need to fit within the curved regions of the cross-section.

Fig. 19(c) shows the influence of the width and number of battens on performance and weight, for a given boom cross-section. Because batten scaling depends significantly on the boom cross-section, we plot two different cross-sections, one with smaller longerons, plotted in blue, and one with larger longerons plotted in red. For both cross-sections, increasing the number of battens initially improves bending performance. However, beyond a point, increasing the number of battens further reduces performance. The optimal number and width of battens for a given cross-section shape can be expressed in terms of the percent of the boom length occupied by battens, or the number of

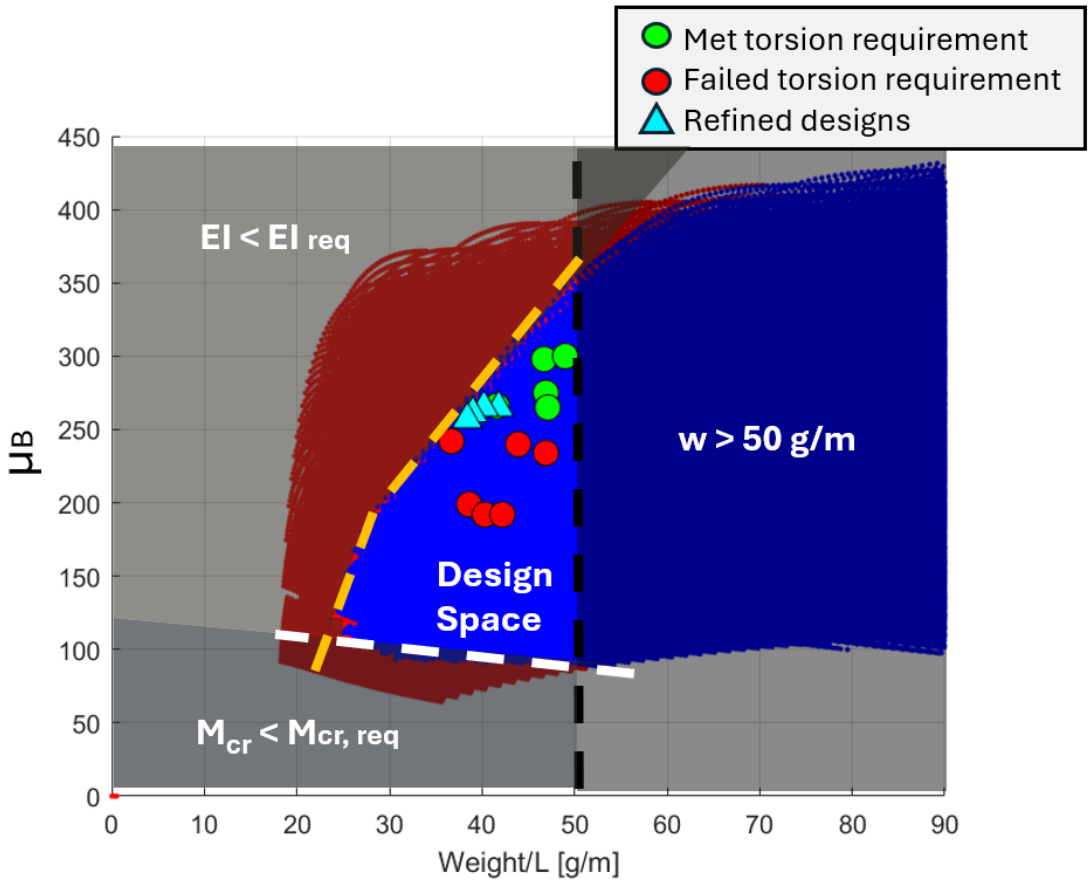

Fig. 17 Mass per unit length plotted against bending performance with select designs highlighted

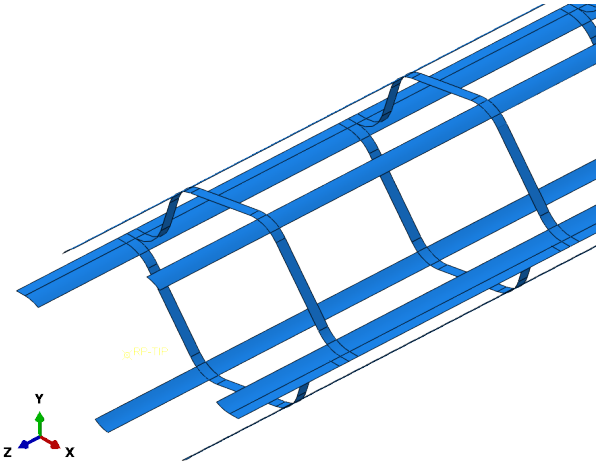

Fig. 18 Boom design candidate visualized in Abaqus

Table 2 Boom Design Candidate Properties

Property	Value
Flange-to-flange distance	5.9 in
Longeron width	0.4 in
Batten width	0.25 in
Number of battens	180
w	38.4 g/m
EI_Y (FE)	3392 Nm^2
Bending $M_{cr,Y}$ (FE)	4.5 Nm
Torsion M_{cr} (FE)	0.104 Nm
Tip deflection at M=0.26Nm (FE)	2.4 cm
μ_{BY} (FE)	241

battens times batten width divided by boom length. For the cross-section with smaller longerons, 19% coverage leads to maximum performance, while for larger longerons maximum performance is achieved at 48% coverage.

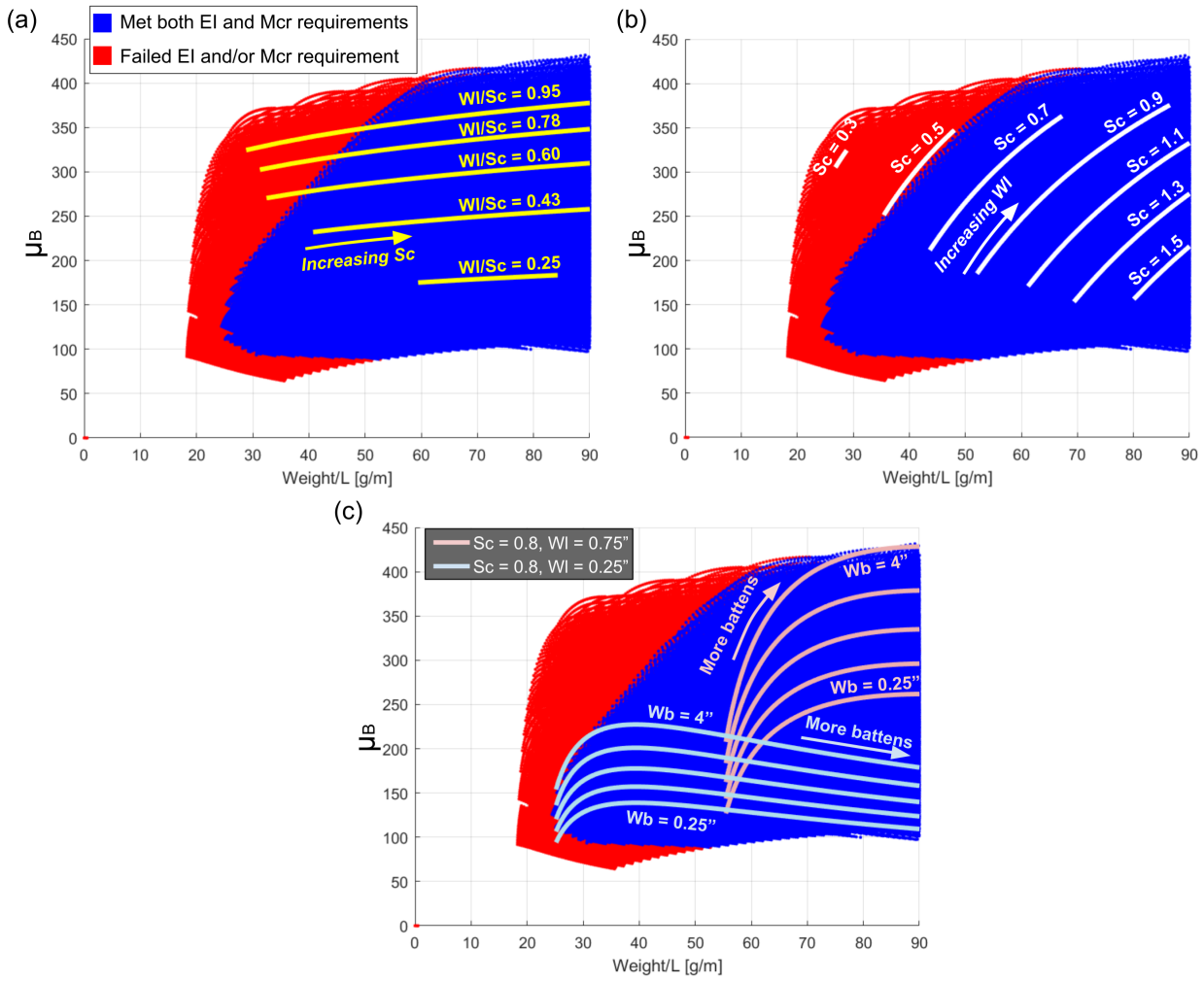

Fig. 19 Boom bending performance plotted against mass per unit length evaluating (a) the effect of uniformly scaling the boom cross-section for constant ratios between the longeron width and scaling factor, (b) the effect of increasing longeron width given a constant scaling factor, and (c) the effect of increased batten width and number of battens which also depends significantly on longeron width.

VI. Conclusions and Plans for Future Research

This work presented finite element simulations and approximate closed form solutions for bending stiffness and bending critical buckling moment, which served to constrain the design space for the SSTM. These models provide insight into which design variables influence homogenized beam properties, as well as the underlying mechanism behind more complex behavior like periodic local longeron buckling. A scalability study revealed that increasing longeron width improves the boom's bending performance with a lower weight cost than scaling the entire cross-section.

Analysis of axial buckling revealed that global buckling modes occur at significantly lower loads than local modes for a target boom length of 27 m. Results also showed that the SSTM undergoes non-negligible shear deformation, and thus the Timoshenko beam model better predicts FE results than the more often used Euler-Bernoulli model. However, it was found that for the mast lenght and boundary conditions of interest, the Euler-Bernoulli model converges with the Timoshenko model and agrees with FE results. This gives us confidence that we can use the boom bending stiffness and the expected C/L ratio determined by the sail vector angle to predict the boom's axial buckling response.

For cantilever bending, shear deformation of the SSTM means that tip deflection is greater than would be predicted by bending stiffness alone using the Euler-Bernoulli beam model. With the Timoshenko beam model, tip deflection

can be more accurately predicted. Anisotropy of the beam leads to out-of-plane deflection. However, expected tip deflections for current design candidates are well within requirements from the system-level model.

While the analytical model presented here for the critical buckling moment in bending for the SSTM served as a helpful design guideline, the model could be further refined to predict boom behavior at a wider range of design variables. However, for the expected bending moments and torsional moments on the SSTM from system-level models, torsion becomes the limiting factor. That is to say, designs which meet torsion requirements also meet moment requirements. Thus, priority is not placed on refining the model for bending buckling moments.

Upon selecting a small number of boom design candidates, we plan to conduct more thorough FE analyses on the SSTM model. In particular, we are interested in evaluating combined loading scenarios, modeling more realistic boundary conditions, and looking for nonlinear buckling behavior. Refining boundary conditions includes both the manor in which load is transferred from sail tension to the mast, as well as the interface between the boom and the deployer. Thus far, the design has relied largely on linear eigenbuckling FE results. We plan to run additional nonlinear FE analyses, particularly for combined loading, to determine whether any nonlinear material or structural effects reduce stiffness or critical buckling loads. This could also include seeding initial geometric imperfections in the FE model, which may indicate the need for additional knockdown factors to be applied for the design.

Acknowledgments

Funding from NASA STTR Program, contracts 80NSSC22PB129 and 80NSSC24CA027, is gratefully acknowledged. We thank Dr. Jay Warren for helpful discussions and technical input.

References

[1] Block, J., Straubel, M., and Wiedemann, M., "Ultralight deployable booms for solar sails and other large gossamer structures in space," *Acta Astronautica*, Vol. 68, No. 7-8, 2011, pp. 984–992.

[2] Puig, L., Barton, A., and Rando, N., "A review on large deployable structures for astrophysics missions," *Acta Astronautica*, Vol. 67, No. 1-2, 2010, pp. 12–26.

[3] Thomson, M., "Deployable and retractable telescoping tubular structure development," *NASA. Lewis Research Center, The 28th Aerospace Mechanisms Symposium*, 1994.

[4] Murphey, T. W., Turse, D., and Adams, L., "TRAC boom structural mechanics," *6th AIAA Spacecraft Structures Conference*, 2019, p. 1746.

[5] Ancona, E., and Kezerashvili, Y. A., "Recent advances in space sailing missions and technology: review of the 6th International Symposium on Space Sailing," *ISSS 2023*, 2024.

[6] Macdonald, M., Hughes, G. W., McInnes, C. R., Lyngvi, A., Falkner, P., and Atzei, A., "Solar polar orbiter: a solar sail technology reference study," *Journal of Spacecraft and Rockets*, Vol. 43, No. 5, 2006, pp. 960–972.

[7] Kobayashi, K., Johnson, L., Thomas, H., McIntosh, S., McKenzie, D., Newmark, J., Heaton, A., Carr, J., Baysinger, M., Bean, Q., et al., "The high inclination solar mission," *arXiv preprint arXiv:2006.03111*, 2020.

[8] Thomas, D., Kobayashi, K., Mike, B., Bean, Q., Capizzo, P., Clements, K., Fabisinski, L., Garcia, J., and Steve, S., "Solar polar imager concept," *ASCEND 2020*, 2020, p. 4060.

[9] Opterus Research and Design Inc., "Virtual Patent Marking," , Available at: `Pat.opterusrd.com/VPM`. Accessed: December 9, 2024.

[10] Nicholson, L., Folkers, M. W., and Murphey, T. W., "Rollable Composite Boom and Deployer Mechanism Technologies," *AIAA SCITECH 2022 Forum*, 2022, p. 1118.

[11] López Jiménez, F., Sharma, A., Folkers, M., and Murphey, T. W., "Design and Characterization of a Trussed Collapsible Tubular Mast," *AIAA SCITECH 2024 Forum*, 2024, p. 0411.

[12] Murphey, T. W., Francis, W. H., Davis, B. L., Mejia-Ariza, J., Santer, M., Footdale, J. N., Schmid, K., Soykasap, O., Guidanean, K., and Warren, P. A., "High Strain Composites," *2nd AIAA Spacecraft Structures Conference*, 2015, p. 0942.

[13] Sharma, H. S., Rose, T., Seamone, A., Murphey, T., and López Jiménez, F., "Analysis of the Column Bending Test for Large Curvature Bending of High Strain Composites," *4th AIAA Spacecraft Structures Conference*, 2017, p. 0171.

[14] Murphey, T. W., "Booms and trusses," *Recent Advances in Gossamer Spacecraft*, Vol. 212, 2006.

[15] Murphy, D., Murphy, T., and Gierow, P., "Scalable solar-sail subsystem design concept," *Journal of Spacecraft and Rockets*, Vol. 40, No. 4, 2003, pp. 539–547. https://doi.org/10.2514/2.3975.

[16] Timoshenko, S., and Gere, J. M., "Theory of Elastic Stability," *Theory of Elastic Stability*, Second Edition, Dover Publications Inc., Mineola, NY, 1961.

[17] Timoshenko, S., "On the correction for shear of the differential equation for transverse vibrations of prismatic bars," *The London, Edinburgh, and Dublin Philosophical Magazine and Journal of Science*, Vol. 21, No. 245, 1921, pp. 744–746.

[18] Hu, Z., Pan, W., and Tong, J., "Exact Solutions for Buckling and Second-Order Effect of Shear Deformable Timoshenko Beam–Columns Based on Matrix Structural Analysis," *Applied Sciences*, Vol. 9, No. 18, 2019, p. 3814. https://doi.org/10.3390/app9183814.

[19] Soykasap, O., "Analysis of tape spring hinges," *International Journal of Mechanical Sciences*, Vol. 49, No. 7, 2007, pp. 853–860.